

Time-resolved polarimetry over water waves: relating glints and surface statistics

M. Ottaviani,^{1,*} C. Merck,¹ S. Long,² J. Koskulics,¹ K. Stamnes,¹
W. Su,³ and W. Wiscombe⁴

¹Department of Physics & Engineering Physics, Stevens Institute of Technology, Hoboken, New Jersey 07030, USA

²NASA GSFC/WFF, Ocean Science Branch, Wallops Island, Virginia 23337, USA

³Science Systems and Applications, Inc., 1 Enterprise Parkway, Hampton, Virginia 23666, USA

⁴NASA GSFC, Greenbelt, Maryland 20771, USA

*Corresponding author: mottavia@stevens.edu

Received 12 November 2007; revised 6 February 2008; accepted 11 February 2008;
posted 28 February 2008 (Doc. ID 89608); published 1 April 2008

The phenomenon of sunglint, well known in satellite remote sensing, lacks a fundamental characterization under controlled laboratory conditions. Exploiting an apparatus specifically assembled for the purpose, we examine the signal collected by a photopolarimeter, pointed at a wavy water surface with measurable statistics and illuminated by a laser source. We also analyze the wave slope distributions, retrieved with an imaging system, and correlate them with the time series of glints. More particularly, we investigate the link between the occurrence of glints and that of the slopes from which they originate. In this context, the results obtained by applying the Hilbert–Huang transform technique to the slope time series are compared with those obtained through a traditional Fourier transform. This novel study first identifies the individual atomic glints as Fresnel reflection originating from a single wave facet. It then discusses the periodic character of a sequence of glints generated by a gravity wave state, as opposed to the erratic behavior of glints typical of capillary wave states. In mixed gravity–capillary conditions, it is shown that the glint properties are governed mainly by the capillary regime. © 2008 Optical Society of America

OCIS codes: 120.6660, 010.0280, 010.4450.

Because of its wide dynamical range, sunglint is normally regarded as a nuisance in satellite remote sensing applications. For this reason data collected in the sunglint region are discarded as “sunglint contaminated.” Nonetheless, it has been shown [1,2] that this strong signal could in the future provide an exceptional signal-to-noise ratio for direct transmittance measurements of atmospheric constituents using the sunglint patch as a source. The well-known investigation carried out by Cox and Munk [3–5] provides the link between surface roughness and wind speed. It is therefore understandable how an accurate description of the sunlight reflection off water

bodies would benefit the retrieval of atmospheric and oceanic parameters.

To this end a special experimental apparatus was built for the polarimetric study of bidirectional reflectance over a water surface where the surface statistics can be repeatably controlled. The growing interest in polarimetry as a remote sensing tool [6–8] led us to assemble a detector capable of retrieving both intensity and polarization components of the reflected light.

The design presented several challenges. Water waves are dynamic [9–11], and can neither be generated with a compact apparatus nor be tilted at will to realize different illumination conditions, as is done in many reflectance experiments on solid samples to avoid the repositioning of the light source and/or the detector [12]. The mechanical suspension had to be designed around the geometrical constraints

of a wave tank. The design provides stiffness and a convenient, quick positioning method, yet remains lightweight and nonobstructive.

In Section 1 we give a brief description of the apparatus. After a presentation of the general features of glints (Section 2), we employ attractor plots to examine the level of chaoticity for glints generated by different wave states (Section 3). In Section 4 we investigate the connection between the collected time series and the surface statistics derived from the imaging system. We also present the results obtained by applying the Hilbert–Huang transform (HHT) technique [13–15] to the slope time series. Our findings are summarized in Section 5.

1. Experimental Setup

The details of the experimental apparatus (see Fig. 1) are described elsewhere [16]. The following provides a summary.

The wave tank facility is located at the Air–Sea Interaction Research Facility at NASA Goddard Space Flight Center, Wallops Flight Facility, Wallops Island, Virginia [17]. Controlled wave states can be created by means of three independent dynamic forcings: a hydraulic pusher unit at one end of the tank to create gravity waves, which are then absorbed at the other end; a wind generator to create capillary waves; and a subsurface current to improve the simulation of real-world situations. Computer control of wind, current, and hydraulic units allows complete hands-off automation of research runs, as well as accurate repetition of unsteady situations for statistical studies.

A suspended semicircular rail, hereafter referred to as the “rainbow,” was assembled from scratch and mounted with its plane parallel to the long axis of the wave tank (and perpendicular to the floor). On the rainbow a laser source and a detector can be

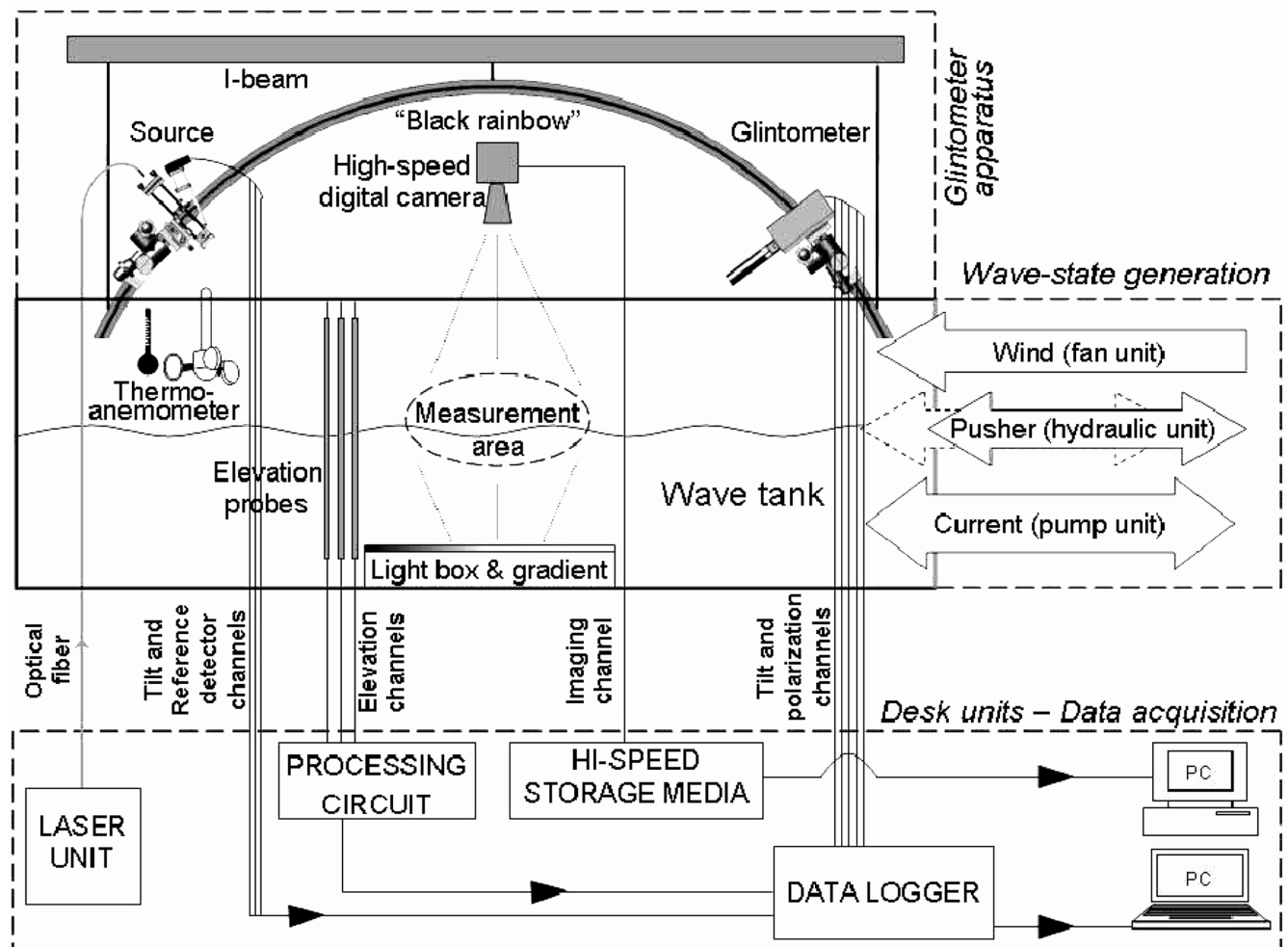


Fig. 1. Block diagram of our glint-measurement apparatus. Wave states in the tank are created by using any combination of the tank control units for wind, wave, and current. The 1 m radius, rainbow-shaped rail with source and detector is here rendered with AutoCAD, and shows the instrumentation positioned at the Brewster configuration (source and detector both at 53.1° from the vertical). The 12-channel datalogger records reflected light (intensity and polarization components, 3 channels), glintometer temperature, reference detector signal, instrument tilt (pitch and roll of both source and glintometer, 4 channels), and wave elevation on capacitance wires spaced 1 cm apart near the glint area (3 channels). Images of the portion of surface under investigation are captured by an imaging system (support not shown for simplicity) and stored in a separate personal computer. Water and air temperature and wind speed are also monitored in each experiment.

locked in position, so that they point at a small area of the water surface at specified polar angles with satisfactory precision. Movement along the rail is accomplished with carriages, equipped with geared heads that allow fine positional and angular tuning. The source is a fiber-optics-coupled laser diode emitting at 635 nm. The incident state of polarization is selected with a linear polarizer. A reference photodiode samples the beam for normalization purposes. The detector ("glintometer") is a custom-built photopolarimeter. A polarizing beam splitter splits the incoming beam to measure the first three components of its Stokes vector [18,19]. High temporal resolution is obtained by employing a fast data logger.

A fast imaging system, with the camera mounted atop the rainbow, captures images of the surface, enabling the retrieval of the wave slope distribution for each wave state under analysis [20]. Vertical capacitance-wire probes [21], partially immersed in the tank, are also used to measure the longitudinal and transverse surface elevation and, from differences in elevation between pairs of wires, the slope. The data from capacitance wires served as a benchmark to establish the adequacy of the calibration procedure used for the imaging system.

The following wave states [22] were considered: (1) the gravity wave state (hydraulic unit driven at 1.25 Hz and 1.3 V peak-to-peak amplitude, resulting in 2.6 cm linear displacement of the piston and 1.5 cm average total wave height); (2) capillary wave state (wind speed $\sim 3.1 \text{ ms}^{-1}$); (3) the combination of the two states above.

During the collection of glint time series, both the source and the glintometer were positioned at 30° from zenith. The spot size of the incident light beam is 3 mm. The glintometer aperture was set to 12 mm, corresponding to a field of view of 3.5° . Under these conditions about 6 cm of surface is observed from zenith [16]. The settings were selected based on previous experience: they prevent multiple reflections and shadowing from taking place. Under these conditions, data runs of 15 min provided a significant number of glints.

2. Glints as Fresnel Reflectance

Before waves were introduced, the apparatus was tested by reproducing the Fresnel equations from measurements of the specular reflection from the flat surface at a range of angles. As seen in Fig. 2, the experimental points show good agreement with the theoretical curves, which quantify the intensity of the polarization components of the reflected light: *s* for the component oscillating perpendicularly to the plane of reflection, *p* for the parallel component. Somewhat surprisingly, an extensive literature search did not reveal any other reported attempt to experimentally confirm the Fresnel equations over a flat water surface. The response of the glintometer at 30° gave reflectance values for the *s* and *p* components of 0.029 ± 0.002 and 0.011 ± 0.001 , respectively. These values compare satisfactorily with

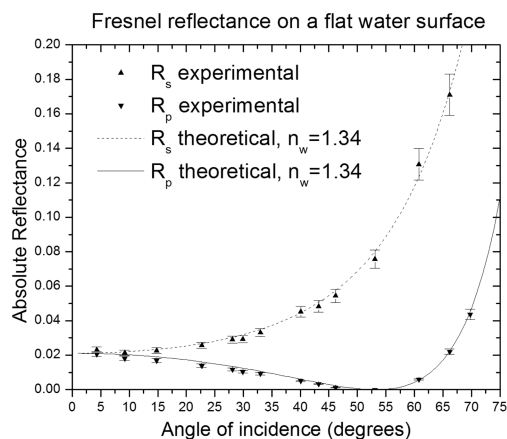


Fig. 2. Measured and theoretical Fresnel reflectance components for a flat water surface. The theoretical curves assume a water refractive index of 1.34. The data are normalized to a reference detector that samples the beam before it leaves the source.

those theoretically predicted (0.032 and 0.012) for a refractive index of water of 1.34, in view of the difficulty in aligning the instrumentation (pitch, roll, and yaw) from a suspended structure. Also, it should be noted that most of the other data points show better agreement with the theoretical curves than the value at 30° . In the presence of waves, the reflected beam will follow trajectories determined by the surface slopes. Glints are observed only when the reflected beam is observed through a limited aperture (in our case the iris placed in front of the instrument baffle). Within the tangent plane approximation, glints occur every time the surface slope is oriented to realize the specular geometry between the source and the detector. If the source and detector are positioned at polar angles θ_s and θ_D , the reflected beam will hit the center of the field of view (FOV) when the incident beam illuminates a portion of the surface tilted at an angle $\beta = \frac{1}{2}(\theta_D - \theta_s)$. The width of the glint peaks, related to the tangential velocity of the reflected beam, depends on the distance of observation.

Throughout the paper, we will refer to glints generated by gravity and capillary wave states as "gravity glints" and "capillary glints," respectively. As an example of how glints are generated, we show the response of the apparatus as the flat water surface is initially disturbed by a train of gravity waves driven down the tank by the hydraulic paddle (Fig. 3). By combining the output from the capacitance wires and the three detectors, we obtain an actual representation of the wave state with the glint intensities overlapped with the slopes at which they occur. In Fig. 3 the source illuminates the water surface at the Brewster angle (53.1° from the vertical), and the detector is specularly positioned at the same angle. In the Brewster configuration only the *s* component is reflected. The constant signal of the Fresnel reflectance on the flat surface is broken down in glints as the first, growing waves modify the surface tilt at the location of the illuminated spot. As expected, glints appear at the same position for each

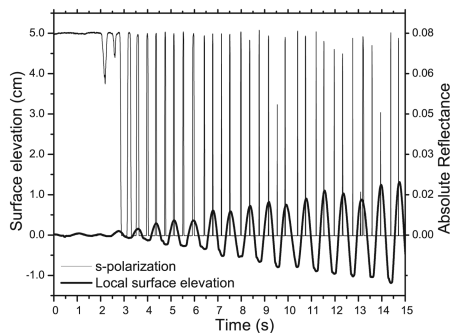


Fig. 3. The flat surface is disturbed as paddle-driven waves (thick black curve) start running down the tank. The axis on the left refers to surface elevation measured with capacitance wires and that on the right to the reflectance values measured by the glintometer. There is no wind and therefore no capillary waves in this case. With source and detector at equal angles, the reflected beam enters the FOV only when reflecting from a zero slope (in this case, a crest or a trough). Here only the s -polarization intensity (light gray) is shown, since the p -polarized intensity is basically zero because of the Brewster-angle geometry. Glints whose peaks do not reach the Fresnel reflectance value are due to occasional non-1D waves reflecting partially or totally off the detector FOV.

cycle, i.e., only for that particular slope that exactly realizes the specular reflection conditions between source and detector. In our case ($\theta_S = \theta_D$) glints originate from the flat crests and troughs of the waves. Only the intensity s component is shown, since all the reflected beam intensity is stored therein. From this plot, representative of a situation constantly observed throughout our experiments, it is clear that the glint polarization intensities assume the values predicted by the Fresnel reflectance, as long as the reflected beam fully enters the FOV.

In practice, it is difficult to generate perfect 1D waves traveling down the tank. Cross-tank components, sometimes significant, reflect the incident beam out of the plane containing the source and glintometer, occasionally leading to low-intensity or even totally missing glints.

Modulations in a glint profile occur only as an effect of the FOV. A top-hat glint (a symmetric glint with a plateau) means that the reflected beam traverses the FOV along (or close to) a diameter of the iris. Jagged profiles imply that the reflected beam spends time at the edges of the FOV. It should be mentioned that a spot size of 3 mm covers an area that in the case of capillary waves is comparable with the wavelength of some of the waves. Therefore, blooming of the reflected beam can also be partially responsible for a decrease in the peak intensities of the glints. From these considerations we conclude that the information contained in the polarization channels does not seem to reveal anything other than pure Fresnel reflectance. More specifically, each fully developed glint manifests the polarization components expected for that particular angle of incidence of the laser beam.

3. Glint Chaoticity

To help answer the question of whether glints are due mainly to gravity or capillary waves, we start

the investigation on the glint statistics with a comparison of the glint-to-glint interval distributions. From the collected time series, the glints were extracted by parsing the files with a fast peak-finder routine. A glint flag is triggered every time the intensity rises over a certain threshold set well above the noise level, at which time the glint number, position, and duration are stored. Figure 4 compares the data collected from the three wave states considered. The most striking feature is the organization of the gravity glint intervals into three distinct peaks (0.3, 0.5, and 0.8 s). If the hydraulic paddle generated sinusoidal waves with the same period as the input signal, we would expect evenly spaced glints from each crest and trough, resulting in a dominating peak corresponding to half the period of the driving frequency input to the paddle. However, there is no such peak in the data. Instead, the presence of glint-to-glint intervals at 0.3 and 0.5 s indicates that the underlying wave is not sinusoidal but rather has significant skewness. A peak corresponding to the sum of these intervals (0.8 s) is also observed, due to missed glints, and mirrors the driving frequency of the hydraulic paddle (1.25 Hz = 1/0.8 s). Multiple missing glints in this sequence generate the small peak at an interval twice as long (1.6 s). A few very short intervals are found, due to glints whose peaks are split as a result of their trajectory relative to the FOV.

The two lower panels, depicting the purely capillary and the mixed gravity–capillary wave states, reveal a fundamentally different behavior than does the gravity wave state alone. The faster evolution of the surface slopes causes glints to cluster at shorter intervals. The distributions steadily decay in a similar fashion with the exception of the rather broad peak exhibited by the capillary wave state at about 0.07 s, corresponding to frequencies around 14 Hz. This value reflects the presence of glints originating from crests and troughs of capillary waves oscillating

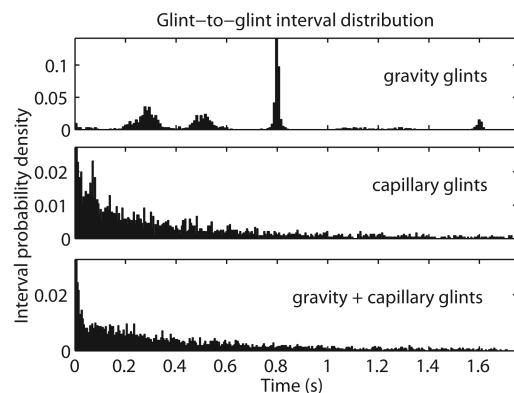


Fig. 4. Glint-to-glint interval distributions for the glints collected under the gravity, capillary, and mixed wave state. The histograms are normalized to 1, so that the ordinate values correspond to the probability of occurrence. Note the dominance of peaks at 0.3, 0.5, and 0.8 s in the discrete spectrum of gravity glints, and the similarity of the two lower panels (capillary and gravity–capillary glints) with the exception of the peak at 0.07 s in the capillary wave state.

at 7 Hz, as confirmed by the component analysis (see Section 5). Interestingly, this peak is suppressed in the mixed wave state. The reason for the loss of this feature is to be sought in the relative system of reference in which the capillary waves move. Purely wind-driven capillary waves are characterized by a range of frequencies. When capillary waves ride on top of gravity waves, nonlinear interactions cause the capillary waves to momentarily accelerate and decelerate with the crests and the troughs of the faster gravity waves. The result is a frequency modulation that redistributes the peak frequencies throughout higher and lower adjacent frequencies and also increases the probability of observing a wider range of slopes.

The distributions of glint durations is also interesting. Figure 5 shows the distribution densities obtained after normalizing the area subtended by the envelopes of the histogram bars. Gravity glints exhibit a primary peak around 0.008 s and a secondary peak around 0.019 s. For a 12 mm aperture the corresponding glint speeds (tangential velocity) are 1.5 ms^{-1} and 0.6 ms^{-1} for observing 1 m away from the surface as in our setup. The angular velocity corresponding to the primary peak, 1.5 rad s^{-1} , corresponds to the rate of slope evolution at the surface at a crest or a trough. A secondary wave component can introduce a near-zero slope region between crests and troughs (see Fig. 6). Since in this region the slope rate of change is slower than at a crest or a trough, the generated glints are longer lived. We attribute the secondary peak in the gravity-glints duration distribution to glints generated under these conditions. The distributions from the remaining two wave states show essentially the same trend, with a predominant duration of 0.002 s (angular velocity equal to 6 rad s^{-1}). This value is once again in agreement with the ratio between typical gravity and capillary wave frequencies.

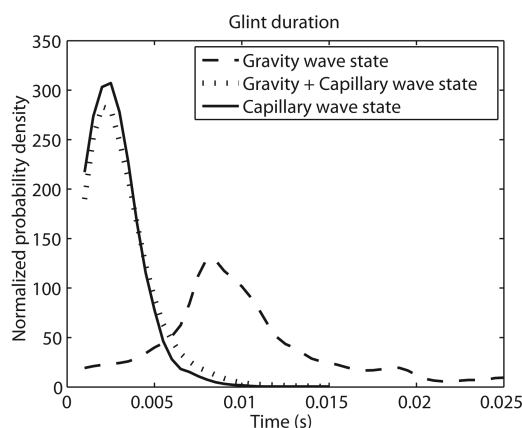


Fig. 5. Normalized probabilities for the glint durations sampled in the three considered wave states. Most of the captured capillary glints last 0.002 ± 0.001 s. The peak in the distribution is well separated from that of gravity glints, which exhibit a broader range of values centered at 0.008 s. The mixed state shows essentially the same behavior as the capillary state.

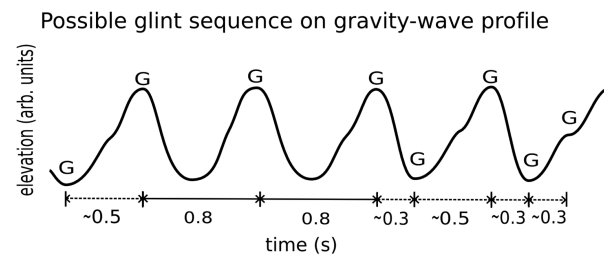


Fig. 6. Schematic illustration of the gravity wave state, as derived from the imaging data. The overall wave profile is pseudo-sinusoidal, with a virtually constant crest-to-crest period mirroring the 1.25 Hz driving frequency of the paddle. A secondary, higher-frequency wave component can interpose an inflection point (with near-zero slope) at a slightly variable location between a trough and a crest and cause variation in the position of the troughs relative to the crests. Source and detector are positioned at the same angle: including the crest and the trough, there are therefore three points per wave period which can potentially generate a glint. However, due to nonzero cross-tank slopes or other variations in the wave profile, glints may not always occur. One possible sequence is shown by the series marked "G". Intervals between adjacent glints are marked along the abscissae. The variability of intervals created by the secondary component is represented by dashed lines and a "~" preceding the duration. In an attractor plot (see Fig. 7), the points contributed by this glint pattern would be $(\sim 0.5, 0.8)$, $(0.8, 0.8)$, $(0.8, \sim 0.3)$, $(\sim 0.3, \sim 0.5)$, $(\sim 0.5, \sim 0.3)$, $(\sim 0.3, \sim 0.3)$.

Graphs like Fig. 4 cannot provide information on the correlation between glint intervals. To analyze this interesting information we utilize attractor plots [23]. Such scatter graphs are used to visualize the level of chaos in a dynamic system by plotting the interval between two occurrences against the previous interval. If a phenomenon occurs at regular intervals, all occurrences will overlap at a single point. For fully chaotic systems, data points will instead be randomly scattered. The presence of patterns (*strange attractors*) reveals different levels of randomness. If the combined wave state (gravity-capillary) shows features closer to the capillary wave state, we can conclude that the signal collected by the glintometer derives primarily from capillary glints rather than from gravity glints.

Figure 7 presents the results for the gravity wave state. A total of nearly 1500 glints are distributed in a very organized pattern. The plot exhibits an intrinsic symmetry about the main diagonal due to reciprocity of intervals (our time series could just as well be analyzed with the temporal axis inverted).

The predominant occurrence is that of alternating ~ 0.5 and ~ 0.3 s intervals, accounting for 26% of the recorded glints. The high peak at $(0.8, 0.8)$ indicates instead that 17% of the glints appear at regular intervals 0.8 s long. It is noteworthy that the feature at $(0.8, 0.8)$ appears sharper than those at $(0.5, 0.3)$ and $(0.3, 0.5)$. The former feature appears more stable experimentally because the driving frequency on the wave tank system is at a stable 1.25 Hz. However, the hydrodynamic effects governing the wave shape and the magnitude of the skewness vary, resulting in a wave shape that evolves in time while the wave-

length remains constant. Thus the features of the attractor plot that depend on the wave shape are blurred, while the features depending only on the wavelength remain crisp.

As suggested earlier, if there were no cross-tank wave components, then only glints separated by 0.5 and 0.3 s would be recorded. However, with nonzero slope components in the cross-tank direction the behavior is more probabilistic. A single glint missing in this sequence generates an interval of 0.8 s followed again by one of either 0.5 or 0.3 s, giving rise to the clusters at (0.8, 0.3), (0.8, 0.5), (0.3, 0.8), and (0.5, 0.8). Together, these clusters amount to 15% of the total number of occurrences. This value is very close to 17%, which is expected since both occurrences are driven by the same event (one glint skipped).

Skipping of glints over one entire wave period, or more, causes the basic pattern to replicate at intervals greater than 0.8 s, but with a much smaller probability. Such features include the small peak at 0.16 s, caused by the missing of glints from two consecutive periods.

A minor feature (10% of occurrences) lies around (0.3, 0.3). These intervals are attributed to the transient overlap of a secondary wave component, of variable phase shift, which can interpose a flat slope roughly halfway between a trough and a crest of the dominant wave.

All the discussed features were replicated by a simple computer simulation. First we adjusted an analytically defined waveform to resemble the wave shape obtained as the time integral of the slope evolution at a representative pixel location. Low random noise was overlapped to the waveform to simulate instrumental and surface noise. From the time series of slopes derived by taking the first derivative, synthetic glints were generated every time the slope was found in a small range around zero. The resulting glint data were then run through the same peak-finding routine as the real data. The resulting attractor plot shows essentially the same pattern found in Fig. 7.

The randomness of the capillary glints is clear and is observed even in the presence of an underlying gravity wave to a level that makes the plots in Figs. 8 and 9 indistinguishable. The erratic movement of the reflected beam is manifested by the increasing density of points toward zero values for the intervals, resulting in rapid passages through the FOV. Although the visibility of features like the characteristic peak of capillary waves is limited by the resolution, Figs. 5–8 confirm that glints generated by the mixed wave state behave much more like capillary glints than like gravity glints.

4. Surface Statistics Investigation

Two systems are available at the wave tank for the measurement of surface slope. The capacitance-wire probes are positioned 1 cm apart, and this separation limits the resolution to the measurement of gravity waves only (capillary waves having wavelengths <1.73 cm and often shorter than 1 cm). To test the ade-

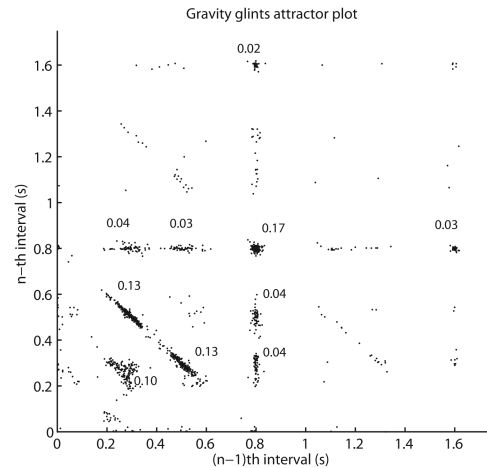


Fig. 7. Attractor plot for glints generated by a gravity wave state. The driving frequency of the hydraulic unit is 1.25 Hz. A total of 1482 glints belong to the dataset. High-density regions are labeled with the fraction of points (intervals) present in the cluster relative to the total number of points in the dataset. A large portion of the intervals (26%) occurs in a 0.5–0.3–0.5 s sequence.

quacy of the imaging system calibration, we compared the distribution derived from the wires and from the camera, finding agreement. This correspondence validates the use of the imaging system for capillary wave states also, where the capacitance wires fail. The imaging system and its calibration have been described by Long and Klinke [20]. The images collected by a digital camera looking vertically down at the surface are meant to provide the statistics of the wave slopes. The surface is illuminated from underwater by a large light box. Each pixel in the image corresponds to a fixed point on the water surface but, as a result of refraction by the local slope, to a variable point on the light box. If the light box provided uniform illumination, the brightness of a point on the surface would remain the same regardless of its slope.

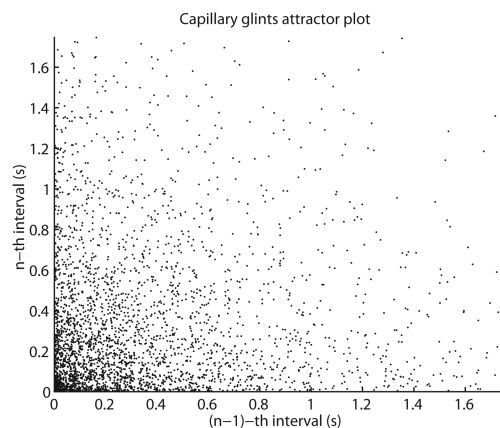


Fig. 8. Attractor plot for glints generated by a capillary wave state. The wind speed is 3.1 m/s. The majority of the 1912 collected glints are scattered throughout the whole interval space below 2 s; only very few intervals (5) were found overlapping at some point. Although the distribution favors shorter intervals, the randomness in the correlation between consecutive capillary glints is evident.

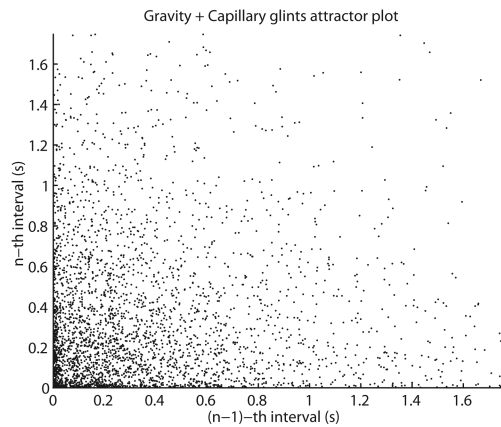


Fig. 9. Attractor plot for glints generated by the overlap between the previous two wave states. The total number of collected glints is 2645, and the scatter plot is essentially indistinguishable from that in Fig. 8.

The box is therefore masked to produce a linear gradient of intensity along the down-tank direction: in this way, the measured intensity is a function of surface slope. It is essential to note that the preferential direction (parallel to the long axis of the tank and to the principal plane for reflection) introduced by the gradient means that the retrieved slope is actually the component of the actual slope along that direction. For the purpose of calibration, a Plexiglas barge is floated across the FOV on the still water surface. The bottom of the barge, rather than being flat, consists of eleven known slopes evenly distributed in the positive and negative domain. This series of triangular waves is fully flooded on the inferior side with water. The response of each pixel to the series of known slopes on the barge is recorded. Interpolation between these data points enables the retrieval of the wave slope values from the pixel brightness measured during the experiments. We image a $8 \times 8 \text{ cm}^2$ portion of the surface, close to the illuminated spot, for 60 s at a rate of 60 frames s^{-1} . Each image can be thought of as a 2D array of slope values. Each pixel presents a time evolution of slopes throughout the series of images acquired while sampling a wave state. It was confirmed that the statistics retrieved at several pixel locations overlap within the experimental errors.

In the observed wave states, both gravity and capillary forces have an input to some extent. The gravity restoring force dominates the paddle waves, with the capillary restoring forces having minimal effect. In capillary regimes the influences of both gravity and capillary waves are present, with the capillary restoring force dominating the shortest wavelengths and gravity dominating the longer wavelengths. In gravity-capillary mixed conditions, the same is true: the paddle waves, dominated by gravity forces, are running through the slower wind-generated waves, which are governed by both capillary and gravity effects. The wind-generated waves will in turn stretch and compress somewhat in wavelength, in response to the underlying oscillations.

Figure 10 displays the normalized wave slope distributions for the considered wave states. The slope time series at a particular location is derived by following the evolution in brightness of the same pixel throughout the time series of images. After verifying that the slope time series at different pixel locations are statistically equivalent, the wave slope distributions were retrieved as a smoothed average of the data collected from six arbitrarily chosen pixels. Gravity waves exhibit a smaller range of slopes, with a maximum value of ± 0.1 corresponding to $\pm 6^\circ$. The double-peaked shape is reminiscent of the probability distribution of a pseudosinusoidal function, but with an abundance of slopes near zero. Peaks in the wave-slope distribution are indicative of the value of the wave-slope at the points of inflection on the underlying wave. These peaks become somewhat smeared by variations in the waves, but are nonetheless visible at slopes of approximately -0.04 and 0.02 . The probability of positive slopes is considerably higher than the negative, because three of the four points of inflection per wave period have positive slopes. This asymmetry is due to the fact that the secondary-component feature occurs only on the leading edge of the waves.

The distributions of the remaining two states are almost indistinguishable. The range of slope is twice as big as the gravity waves, reaching maximum slopes of $\pm 17^\circ$. The capillary waves are possibly showing a slight bias toward positive slopes, perhaps an indication of a certain degree of skewness that was smoothed out in the presence of underlying gravity waves as explained in Section 3.

Due to the finite size of the glintometer FOV, glints are accepted originating from a (small) range of slopes, in our specific case centered around zero. This range was calculated and confirmed experimentally to be ± 0.006 , corresponding to $\pm 0.34^\circ$. Integration of the wave slope distributions within these limits provides the probability of occurrence for the flat surface: retrieved values were 12% for gravity waves and 5% for both the capillary and the mixed wave states. Ideally, these percentages should correspond

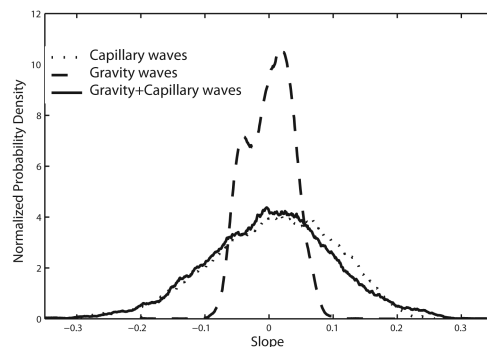


Fig. 10. Normalized wave slope distributions for the wave states under analysis. Note the two predominant peaks in the gravity waves, with an abundance of positive slopes. The capillary and the mixed wave states distributions encompass a wider range of slopes and are practically indistinguishable.

to the fraction of time glints are expected to be observed over the whole data set. Comparing these values with the ratio of the sum of glint durations (total glint-on time) to the total duration of the time series, we found that the imaging system overestimated the expected occurrences. Yet, this discrepancy is largely expected because slope components in the cross-tank direction, when present, divert the reflection away from the plane of the rainbow even though the down-tank component might have a value favorable for glint detection. This effect is significant for capillary waves, but less important for gravity waves, since they are produced mainly with a fetch parallel to the cross-tank direction.

Our imaging system can measure slope components only along the down-tank direction. A complete mapping of the surface is paramount when seeking a quantitative relation between the occurrence of glints and the particular slope from which they originate. A technique that exploits a color gradient rather than a monochromatic one is under development. Measuring the color saturation at each pixel location will enable the retrieval of both down-tank and cross-tank slope components and, by integration, the surface elevation.

Once the calibrated slope images are obtained, they can be analyzed further with the Hilbert–Huang transform (HHT) method established for nonlinear and nonsteady data [13–15]. The application of this method to images has been discussed by Long [24]. Each row of pixels in a calibrated image gives the instantaneous component of the local slope along the down-tank direction. The HHT techniques separate these slope data into scale components, from the shortest (noiselike) to the longest (offsets or slow trends), giving a detailed view of the scales present within the surface area covered by the images. By analyzing a time series of images, the slope distribution during the time of measurement can be obtained, as well as any temporal changes of the water waves' wavelength, slope amplitude, phase, and frequency. In this technique the time scale is not lost, and the resulting joint probability distribution can be simplified into a marginal distribution to give the frequency distribution of slope, a 2D plot that resembles the usual frequency spectrum.

Figure 11 displays the 10 components extracted from 15 s of the sequence of slopes at one pixel location. Adding all 10 components together produces the original time sequence. The most noteworthy components are c4 and c3. The former reveals the presence of the paddle driving frequency at 1.25 Hz; the latter shows the occurrence of slopes at twice this frequency. The first two short-scale slope components are noiselike, with negligible amplitude, and are associated with higher-frequency surface features generated by the paddle waves. Components c5–c10 are also negligible in slope values and are likely to be related to low-level reflections in the tank and nonlinear wave group effects. The last component, being nonoscillatory, was treated as an offset and sub-

tracted from the original time series before further processing.

Figure 12 shows the results relative to the capillary state. In this case the components with heavier weight are c1 and c2. Components c3 and c4, at a lower slope amplitude, show the shift of the wind waves into the lower frequency range, with evident wave groups associated with a growing nonlinear regime. Even though some of the remaining components reveal periodic oscillations, their amplitude is too small to influence the chaotic regime. Once again, the last component was subtracted. The gravity–capillary mixed wave state is depicted in Fig. 13. The short-scale features are similar to those found in Fig. 12, but now all the components from c1 to c5 contribute significantly, as expected from the superimposition of the two states. Component c5 best represents the 1.25 Hz underlying paddle wave, reduced slightly in amplitude as compared with component c4 of Fig. 11, with wave groups forming in response to the interactions with and among the wind-generated waves.

Once the components appearing in Figs. 11–13 are obtained, the HHT technique can produce joint probability distributions and, by summing data along the time axis, marginal distributions that give the distributions of slope and slope magnitude in frequency space. Figure 14 compares the results obtained by applying the HHT and the fast Fourier transform (FFT) techniques.

The paddle frequency of 1.25 Hz can be seen in the upper two graphs where the paddle waves are present, detected by both the FFT and the HHT. One point revealed by the HHT is that frequencies are not steady, which is expected when nonlinear processes take place. As a result, the HHT result is characterized by broadened peaks as opposed to the more discrete distribution found with the FFT. There are also excursions around the second harmonic (2.5 Hz), corresponding to processes occurring at both the crest and trough (therefore twice within the primary paddle wavelength) or at other half-wave locations. The bottom chart exhibits a much more uniform distribution, centered about the peak at 6.5 Hz, which can be considered the characteristic frequency of our capillary wave state for the chosen wind and fetch.

The most interesting feature is perhaps to be found in the gravity–capillary mixed wave state. The capillary distribution undergoes a shift toward lower frequencies, closer to those of the gravity waves on which they are generated. Also, the presence of wind strengthens the processes associated with the second-harmonic frequency, which grows from one third to twice the peak value of the dominant frequency. Curiously though, the FFT suggests an excitation of higher-order harmonics of the paddle frequency not clearly distinguishable in the HHT profile. This effect can be expected in nonlinear regimes, where the assumptions made in applying the FFT (mainly the assumptions of a stationary and linear system of infinite duration) are not fulfilled [13]. As a consequence, higher harmonics are invoked to fit transient

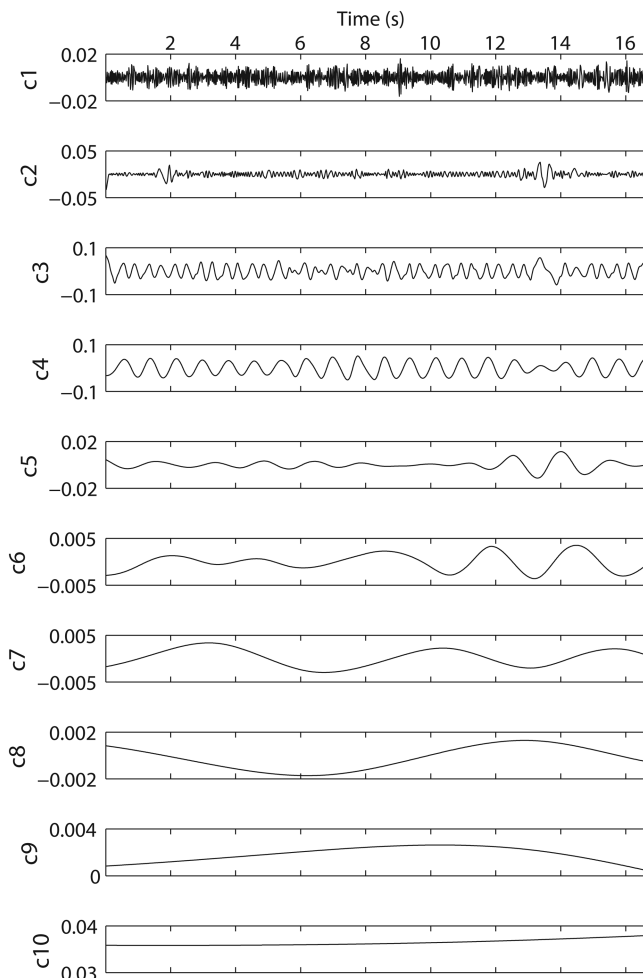


Fig. 11. 15 s of the 10 components extracted from the gravity slope time series with the HHT technique. The ordinate axes are in slope units, and adding all these components yields the complete time series (see text). Note the periodic oscillations found in component c3 and c4.

phenomena and nonlinear effects such as the peakedness of the gravity wave crests, the flattening of their troughs, and the periodic acceleration or deceleration of capillary waves overlapping to them. In contrast, the HHT adjusts to the data without any *a priori* assumptions, and produces a continuous spread in frequencies, which in our view mirrors in a better way the variability of the components. The frequency variability itself can be seen as a function of time in the full joint probability distribution before it is compressed into the marginal distribution form.

Last, we note that the HHT reveals in the top two panels the presence of subharmonics at 0.6 Hz, apparently missing in the FFT plot. This fact illustrates one of the main differences between the two approaches. The HHT will detect a single occurrence of a phenomenon within the dataset, while the FFT depends upon sinusoidal recurrence to register it at all. The observed subharmonic may be attributed to transient reflectance effects within the tank.

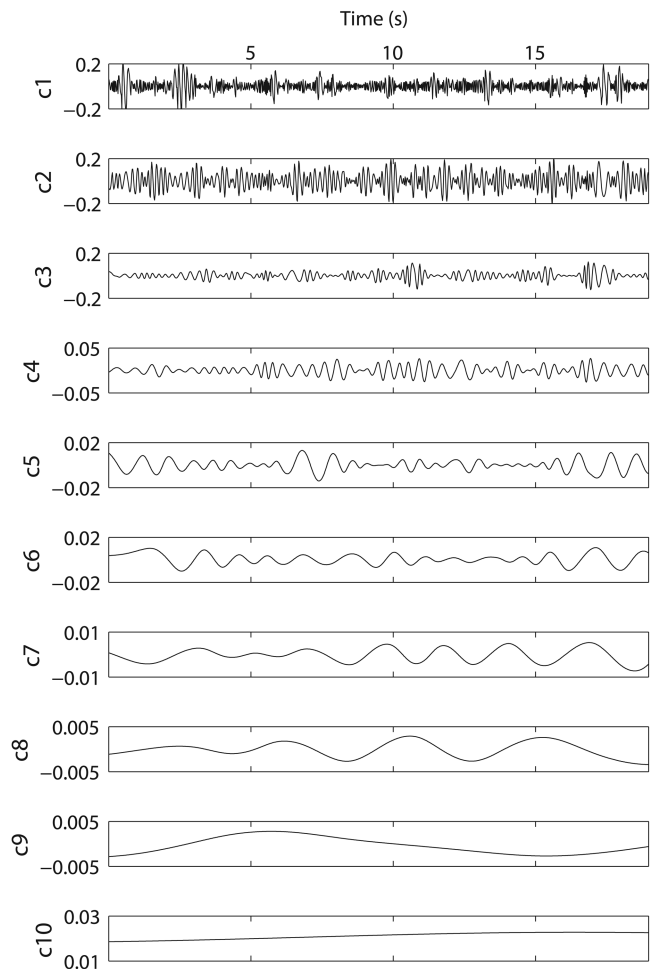


Fig. 12. Same as in Fig. 11, but for the capillary slopes time series.

5. Conclusions

In this study we have analyzed the reflection of a laser beam from a wavy water surface whose statistics are measured by an imaging system. The data show that glints occur whenever the local slope is oriented so as to realize the specular geometry between source and detector. The polarimetric response confirms that the reflected beam carries the characteristic signatures of Fresnel reflectance for the particular geometry of incidence and reflection. Any deviations are due solely to the FOV of the detector. The trajectory and the finite diameter of the reflected beam, which may not enter the instrument aperture completely, are responsible for glints that do not reach the expected Fresnel intensity. Time spent at the edges of the FOV result in modulation of the glint profile. Displaying the glint time series with attractor plots revealed the fundamental difference of the reflection from gravity (periodic) and capillary (statistics-governed) wave states. The overlap between these states generates glints that essentially behave like capillary glints, although a broad feature at 14 Hz, originating from the capillary regime, is dispersed by the gravity wave motion between adjacent frequencies.

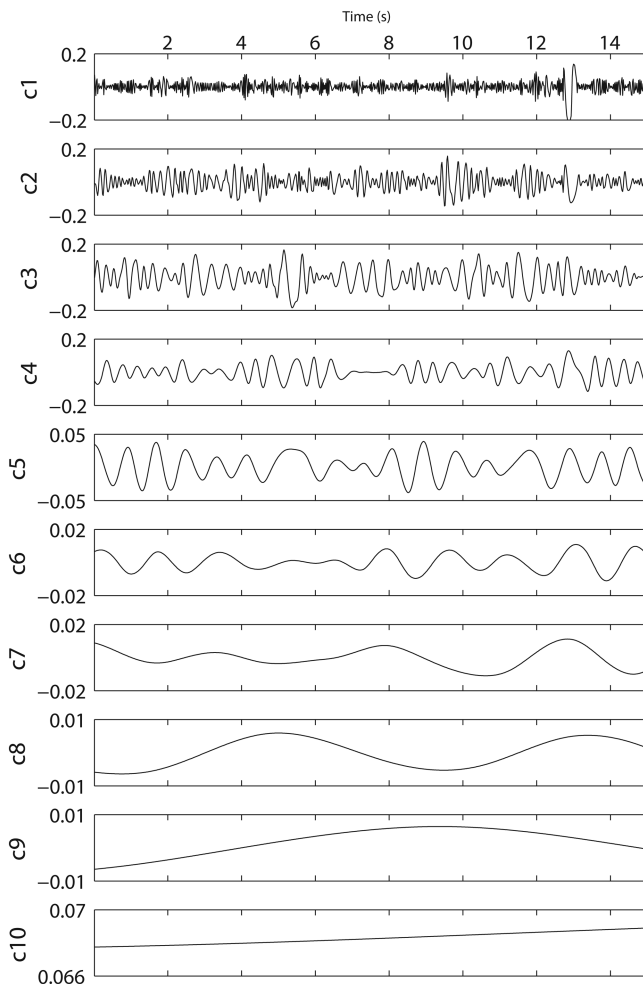


Fig. 13. Same as in Figs. 11 and 12, but for the gravity–capillary slopes time series.

From the slope time series retrieved with the imaging system we were able to simulate all the salient features appearing in glint attractor plots, which not only display the glint-to-glint interval distribution, but also carry information about the correlation be-

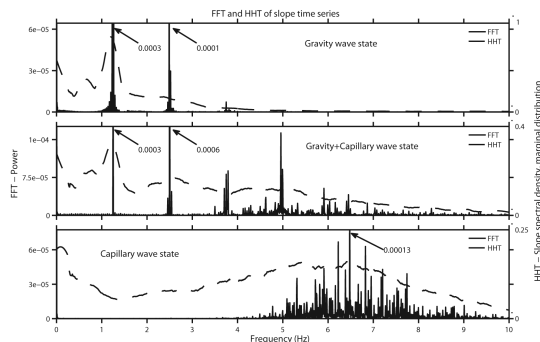


Fig. 14. Comparison of the HHT (dashed curve, right y axis) and the Fourier transform (solid curve, left y axis) of the slope data. The distinct features of the gravity wave wave state (upper panel) contrast with the more uniform distribution typical of capillary waves (lower panel). The central panel represents the overlap between the two states. The arrows report the value of the peaks out of scale.

tween consecutive intervals. While the capillary and the gravity–capillary wave states exhibit a high degree of chaoticity, the interpretation of more deterministic systems like that of the gravity glints was particularly successful.

The HHT can isolate the different scale components of the slope time series. An analysis of the considered wave states, based on the application of this technique to the data retrieved with the imaging system, indicated the similarity between the statistics of capillary and gravity–capillary wave states, revealing on the other hand the much greater degree of periodicity expected for the gravity waves. While the FFT relies on steady and linear periodicity throughout a whole data set to correctly interpret a time series, the HHT provides a physically more meaningful characterization of the transient phenomena and the variability of the wave components typical of a nonlinear, nonstationary system as the one under investigation.

A few aspects differentiate our experimental conditions from the real-world situation in which sunglint is observed from a satellite. First of all, the Sun is a source of broadband, unpolarized radiation. Moreover, the Earth's oceans are not a monodimensional wave tank (although Cox and Munk measured minimal dependence of the wave slope distribution on the wind direction). Most important, the signal captured by a satellite is the result of an average over time and space of glints whose duration is many orders of magnitude shorter because of the much larger surface–satellite distance.

Our apparatus, the first of its kind, proved nonetheless essential in sampling atomic glints, the fundamental entities of which the sunglint patch is composed. Natural extensions of this work, more closely devoted to remote sensing applications, will involve changing the illumination conditions to an unpolarized and large-diameter beam, so as to better mimic typical Sun–ocean situations.

This work was supported by a grant from the NASA Earth Observing System (EOS) program. We acknowledge the invaluable help provided by the NASA Goddard Sciences and Exploration Directorate, which supports the Wallops wave tank facility. We also thank the two reviewers, whose insightful suggestions greatly improved the quality of the manuscript.

References

1. Y. J. Kaufman, J. V. Martins, L. A. Remer, M. R. Schoeberl, and M. A. Yamasoe, "Satellite retrieval of aerosol absorption over the oceans using sunglint," *Geophys. Res. Lett.* **29**, 1928, doi:10.1029/2002GL015403 (2002).
2. R. Kleidman, Y. Kaufman, B. Gao, L. Remer, V. Brackett, R. Ferrare, E. Browell, and S. Ismail, "Remote sensing of total precipitable water vapor in the near-IR over ocean glint," *Geophys. Res. Lett.* **27**, 2657–2660 (2000).
3. C. Cox and W. Munk, "Measurement of the roughness of the sea surface from photographs of the sun's glitter," *J. Opt. Soc. Am.* **44**, 838–850 (1954).
4. C. Cox and W. Munk, "Statistics of the sea surface derived from sun glitter," *J. Mar. Res.* **13**, 198–227 (1954).

5. C. Cox and W. Munk, "Slopes of the sea surface deduced from photographs of sun glitter," *Bull. Scripps Inst. Oceanogr.* **6**, 401–488 (1956).
6. S. Bouffières, F. M. Bréon, D. Tanré, and P. Dubuisson, "Atmospheric water vapor estimate by a differential absorption technique with the polarisation and directionality of the Earth reflectances (POLDER) instrument," *J. Geophys. Res.* **102**, 3831–3842 (1997).
7. P. Goloub, D. Tanré, J.-L. Deuzé, M. Herman, A. Marchand, and F.-M. Bréon, "Validation of the first algorithm applied for deriving the aerosol properties over ocean using the POLDER/ADEOS measurements," *IEEE Trans. Geosci. Remote Sens.* **37**, 1586–1596 (1999).
8. B. Gérard, J.-L. Deuzé, M. Herman, Y. J. Kaufman, P. Lallart, C. Oudard, L. A. Remer, B. Roger, B. Six, and D. Tanré, "Comparisons between POLDER 2 and MODIS/Terra aerosol retrievals over ocean," *J. Geophys. Res.* **110**, D24211 (2005).
9. S. R. Massel, *Ocean Surface Waves: Their Physics and Prediction*, Vol. 11 of Advanced Series on Ocean Engineering (World Scientific, 1996).
10. M. Banner, J. Gemmrich, and D. Farmer, "Multiscale measurements of ocean wave breaking probability," *J. Phys. Oceanogr.* **32**, 3364–3375 (2002).
11. N. Scott, E. Hara, T. Walsh, and P. Hwang, "Observations of steep wave statistics in open ocean waters," *J. Atmos. Oceanic Technol.* **22**, 258–271 (2005).
12. L. Zhao, K. Nielsen, J. K. Lotsberg, E. Marken, J. J. Stamnes, and K. H. Stamnes, "New versatile setup for goniometric measurements of spectral radiance," *Opt. Eng.* **45**, 053606 (2006).
13. N. Huang, Z. Shen, S. R. Long, M.-C. Wu, H. H. Shih, Q. Zheng, N.-C. Yen, C. C. Tung, and H. H. Liu, "The empirical mode decomposition and the Hilbert spectrum for nonlinear and non-steady time series analysis," *Proc. R. Soc. London A* **454**, 903–995 (1998).
14. N. E. Huang, Z. Shen, and S. R. Long, "A new view of nonlinear water waves: the Hilbert spectrum," *Annu. Rev. Fluid Mech.* **31**, 417–457 (1999).
15. N. Huang, M. Wu, S. Long, S. Shen, W. Qu, P. Gloersen, and K. L. Fan, "A confidence limit for the empirical mode decomposition and Hilbert spectral analysis," *Proc. R. Soc., Lond. A* **459**, 2317–2345 (2003).
16. M. Ottaviani, K. Stamnes, J. Koskullics, H. Eide, S. Long, W. Su, and W. Wiscombe, "Light reflection off water waves: suitable setup for a polarimetric investigation under controlled laboratory conditions," *J. Atmos. Ocean. Technol.* (to be published).
17. S. Long, "NASA Wallops flight facility air–sea interaction research facility," NASA Ref. Pub. 1277 (NASA Wallops, 1992).
18. R. Azzam, "Division-of-amplitude photopolarimeter (DOAP) for the simultaneous measurement of all four Stokes parameters of light," *J. Mod. Optic.* **29**, 685–689 (1982).
19. R. Azzam, "Beam splitters for the division-of-amplitude photopolarimeter (DOAP)," *J. Mod. Optic.* **32**, 1407–1412 (1985).
20. S. Long and J. Klinke, *A Closer Look at Short Waves Generated by Wave Interactions with Adverse Currents* Vol. 127 of Geophysics Monograph Series: Gas Transfer at Water Surfaces (American Geophysical Union, 2002), pp. 121–128.
21. S. Long, "A self-zeroing capacitance probe for water wave measurements," NASA Ref. Pub. 1278 (NASA Wallops, 1992).
22. O. M. Phillips, *Dynamics of the Upper Ocean*, 2nd ed. (Cambridge U. Press, 1977),
23. H. Núñez Yépez, A. Salas Brito, C. Vargas, and L. Vicente, "Chaos in a dripping faucet," *Eur. J. Phys.* **10**, 99–105 (1989).
24. S. Long, "Applications of HHT in image analysis, in *The Hilbert–Huang Transform and its Applications*, N. Huang and S. Shen, eds. (World Scientific, 2005), Vol. 5, p. 289.